Journal of the Optical Society of Korea

Vol. 8, No. 1 March 2004

Perspectives on THz Time Domain Spectroscopy

R. Alan Cheville

School of Electrical and Computer Engineering, Oklahoma State University,
Stillwater, OK 74078, USA

Optical Society of Korea

Journal of the Optical Society of Korea, Vol. 8, No. 1, March 2004, pp. 34-52 <Invited>

Perspectives on THz Time Domain Spectroscopy

R. Alan Cheville*

School of Electrical and Computer Engineering, Oklahoma State University,
Stillwater, OK 74078, USA

(Received December 12, 2003)

Over the past decade the experimental technique of THz time domain spectroscopy (THz-TDS) has proved to be a versatile method for investigating a wide range of phenomena in the THz or far infrared spectral region from 100 GHz to 5 THz. This paper reviews some recent results of the Ultrafast THz Research Group at Oklahoma State University using THz-TDS as a characterization tool. The experimental technique is described along with recent results on THz beam propagation and how THz beam profiles arise from propagation of pulse fronts along caustics. To illustrate how spatio-temporal electric field measurements can determine material properties over a wide spectral range, propagation of THz pulses through systems exhibiting frustrated total internal reflection (FTIR) are reviewed. Finally two potential metrology applications of THz-TDS are discussed, thin film characterization and non-destructive evaluation of ceramics. Although THz-TDS has been confined to the research laboratory, the focus on application may stimulate the adoption of THz-TDS for industrial or metrology applications.

OCIS codes : 320.7160, 300.6270, 320.5550, 120.4640, 070.2580

I. INTRODUCTION

We are approaching what some scientists and engineers are dubbing the “Tera-Era” [1]. This vision encompasses state-of-the-art computers performing operations at rates of teraflops, communications systems operating over a single fiber at rates of terabits per second, and electronic devices responding on time scales of 10^{-12} seconds. Although a roadmap which will guide technology to this tera-era is still lacking, there are significant hurdles in moving current devices into this realm. For example, the spectral region from 300 GHz ($\lambda = 1$ mm) to 10 THz ($\lambda = 30$ μm) has been one of the last to see extensive development due to the difficulty of achieving these frequencies by optical or electronic means. The THz spectral region, figure 1, corresponds to a sizable portion of the electromagnetic spectrum. Traditionally this spectral region has been accessed by frequency mixing, far infrared gas lasers, and Fourier Transform Spectroscopy. The challenges and successes in this area have been thoroughly reviewed (see reference [2] and references 1-11 therein).

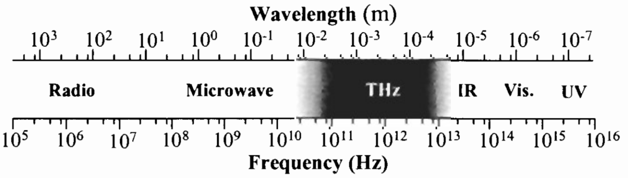

FIG. 1. Diagram of the THz spectral region accessed by THz-TDS lying between electronic and optical regimes.

Much of the work at THz frequencies has been in search of efficient, CW local oscillators with technologically useful power outputs (approximately -10 dBm) [3]. Recent developments in laser diodes, HEMTs, quantum cascade lasers, and difference frequency generation, show this is an achievable goal. However, despite the fact that both electronics and optics are pushing their boundaries into the far infrared region, an alternative approach in use for over fifteen years involves a synthesis of ultrafast optical and electronic techniques to generate sub-picosecond electromagnetic pulses, [4-8] Freely propagating electromagnetic pulses are generated by optically gating a dipole antenna with a subpicosecond laser. The so-called THz pulses are quasi-optical [9] and can be propagated through free space in a well collimated beam, coupled efficiently into waveguides, or confined to micron scale transmission lines. THz pulses have continuous bandwidths that extend from microwave to far-infrared optical frequencies.

This paper provides a brief overview of how THz pulses are finding a unique niche in terahertz tech nology. In certain applications, such as electromagnetic scattering, the localization of energy into a pulse provides insight into the physical mechanisms which are obscured by a frequency domain analysis. For spectroscopic applications, such as materials characterization, the ability to directly measure the electric field of a THz pulse, rather than the intensity envelope, allows an unparalleled tool for measurement of the electronic properties of materials. The next section introduces the experimental technique of THz time domain spectroscopy (THz-TDS) with emphasis on recent work examining characteristics of pulse coupling and propagation. The third section provides a brief theoretical background of THz-TDS materials characterization, utilizing frustrated total internal reflection to illustrate the unique characterization abilities of THz-TDS. Next several applications of THz-TDS are examined including thin film characterization, and non-destructive evaluation of ceramics using electromagnetic scattering. Throughout this paper in-depth examples are used rather than attempting a comprehensive review of THz technologies. A brief summary of other review articles is given in the conclusion.

II. EXPERIMENTAL INSIGHTS

THz time domain spectroscopy utilizes the experimental setup shown in figure 2 (a). In brief the THz source is a DC biased semiconductor which is irradiated with focused ultrafast (< 100 fs) laser pulses. Optical generation of photocarriers in a region of extremely high, trap enhanced electric field [10], and the subsequent acceleration of the carriers, generates the burst of THz radiation which is then collimated by a crystalline silicon lens attached to the back side of the chip. A quasi-optical system is used to couple the THz pulse to an optically gated detector. The THz beam is detected by an optically gated micron scale dipole antenna fabricated on an ion-implanted silicon-on-sapphire (SOS) wafer with sub picosecond carrier lifetime. The electric field of the focused incoming THz radiation induces a transient bias voltage across the receiving antenna. Since current only flows in the antenna structure when the optical gating pulse is present, the time dependent amplitude of this transient voltage is obtained by measuring the collected charge (average current) versus the time delay between the THz pulses and the optical gating pulse.

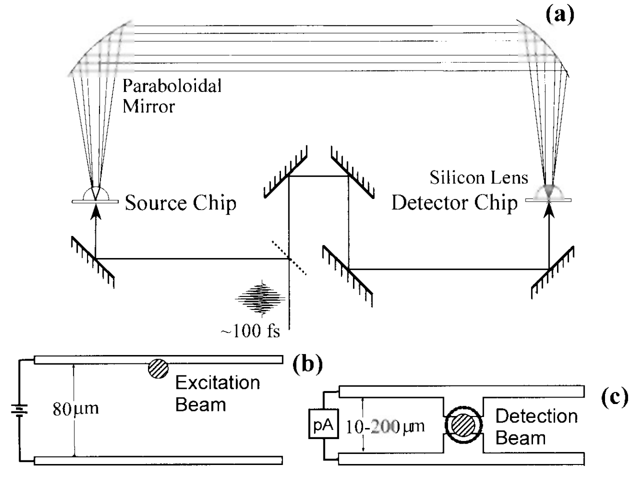

FIG. 2. (a) Experimental system used for THz-TDS. Figure (b) shows the geometry of the THz source photolithographically fabricated on semi-insulating GaAs. (c) is the THz detector dipole which is fabricated on ion implanted SOS.

1. The THz Source

The most common structure used generation of THz radiation is coplanar transmission lines fabricated on a semiconductor with high mobility, typically GaAs. A typical optoelectronic source chip [11] is shown in figure 2 (b). The simple coplanar transmission line structure consists of two 10 μm-wide metal lines separated by 80 μm, fabricated on high-resistivity GaAs, and DC biased at 80V. Irradiating the metal-semiconductor interface (edge) of the positively biased line with focused ultrafast laser pulses produces synchronous bursts of THz radiation. This occurs because each laser pulse creates a large number of photocarriers in a region of extremely high (trap enhanced [10]) electric field. The consequent acceleration of the carriers generates the burst of radiation. A mode-locked Ti:sapphire laser provides 820 nm, 70 fsec excitation pulses with an average power of 5 to 50 mW at the 5 μm diameter excitation spot. The major fraction of the laser generated burst of THz radiation is emitted into the GaAs substrate in a cone normal to the interface; the resulting radiation pattern has been calculated analytically [12]. The THz radiation is then collected and collimated by a crystalline silicon lens attached to the back side of the chip. The lens is a truncated 10 mm diameter silicon sphere cut such that the ultrafast antenna is located at the focus of the lens. Other lens configurations have been used [13] which will be discussed subsequently.

The electric field pattern of the lens-coupled dipole antenna, figure 3 (a), determines the quasi-optical propagation characteristics of the THz beam. The electric field distribution of the THz pulse at a given point in free space is determined by diffraction of the electric field distribution on the silicon lens [13-15], in turn determined by the electric field pattern of a dipole radiator at a planar dielectric boundary. Both the spatial power distribution of a dipole radiator near a plane dielectric interface and the vectorial electric field

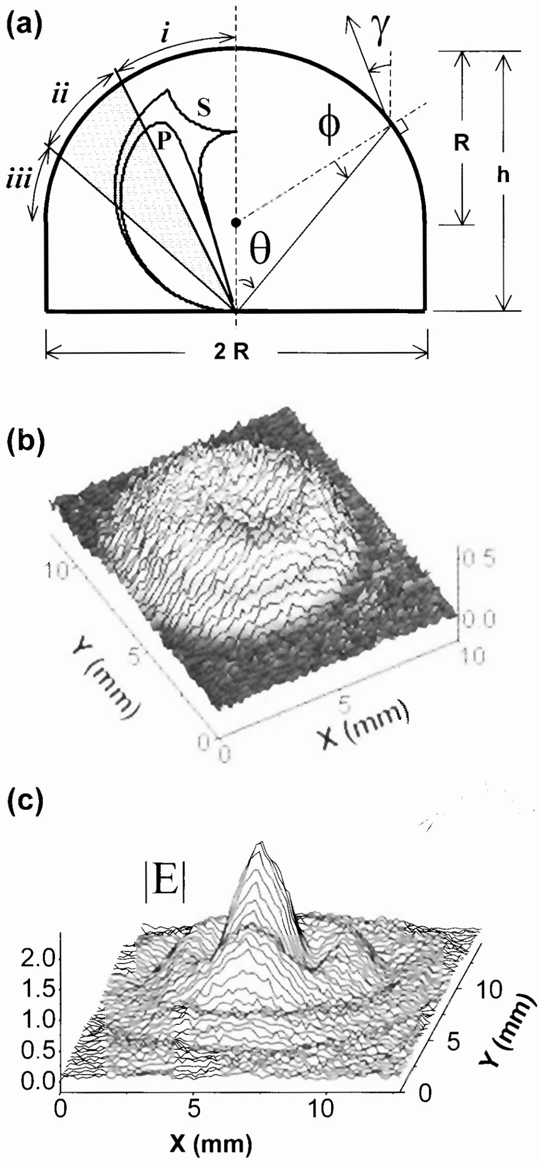

FIG. 3. (a) Detail of the collimating silicon lens. The left half of the figure illustrates regions *i*, *ii*, and *iii* corresponding to direct rays, marginal rays, and surface waves and the field patterns for S and P polarization. The right half of the figure defines angles used in time-of-flight analysis. (b) Measured THz beam amplitude profile, 0.38 THz, at frequency-independent image plane. (c) Spatially resolved electric field amplitudes at 0.38 THz measured at distance d = 16 mm. The inset is the calculated beam profiles.

distributions have been calculated analytically [16,17]. A simpler method to determine the dipole radiation is through a summation of plane waves directly radiated from the dipole and those reflected from the planar substrate-air interface. The reflected waves acquire a angle dependent phase shift caused by total internal reflection, creating the antenna patterns for S and P field polarization shown in figure 3 (a). The phase shift also results in change in polarization from linear to elliptical.

The field external to the silicon lens is determined from the internal field by the Fresnel transmission coefficients [18]. The field along the dipole axis is preferentially coupled out of the lens since it strikes the lens surface near Brewster's angle, $\theta_B = 16.3^\circ$. This leads to a toroidal field pattern external to the lens surface, which has been measured by imaging this field on a movable THz antenna without a coupling lens [19], discussed subsequently. This measurement is shown in figure 3 (b) corresponding to a frequency of 0.38 THz. While the external field pattern is independent of frequency in the plane wave approximation, diffraction serves to smear the toroidal field pattern, especially for low frequencies.

The far field pattern created by the toroidal pattern on the lens surface can be calculated relatively simply, but tediously, from the scalar field on the lens surface using the Kirchoff-Fresnel diffraction integral [20]. This calculation leads to a characteristic Gaussian like structure with a strong central lobe surrounded by Airy-like rings, measured in figure 3 (c) at a distance of 16 mm from the THz source. The calculated beam profile determined from numerical diffraction calculations of the toroidal beam profile external to the lens is shown in the inset. While at tens of mm from the lens the beam exhibits much structure, at distances of tens of cm from the THz source the ring structure is severely attenuated, and the field pattern resembles a $TEM_{0,0}$ Gaussian. This is an important first-order approximation since the ABCD formalism [21,22] can be applied to determine temporal beam reshaping [23,24].

While the ABCD formalism provides a simple and mathematically tractable approach to calculate the effect of any paraxial optical system on a THz beam, it is important to note it is only a first order approximation. Measurements of the complex spatial amplitude distribution of optoelectronically generated THz beams indicate that the beam does not behave like a TEM_{00} Gaussian, particularly in the near field or in image planes, which must be considered in applications of lens coupled THz sources where field patterns are important, such as ranging or coupling into waveguides. The complex field pattern also affects the propagation of THz beam which are less divergent than predicted by a simple $TEM_{0,0}$ approximation. The THz beam profile can be represented as a sum of approximately 50 Laguerre-Gauss modes which accurately predicts propagation of the complex beam profile [19]. However extracting the lowest order, $TEM_{0,0}$, mode accurate predicts the spatial dimension, but not shape, of a freely propagation THz beam.

2. Time Domain Analysis of THz Beam Profiles

To gain a more intuitive understanding of the some of the origins of THz beam profiles, it is helpful to examine how the concentric ring pattern of figure 3 (c) arises using a time-domain analysis. The time domain analysis, while not mathematically rigorous, illustrates how a physical understanding of some phenomena can be enhanced by examining how they arise in the time domain. While the following paragraphs constitute a small diversion from main aim of this section, describing the experimental system used for THz-TDS, they give an intuitive picture of how complex beam profiles can arise.

The concentric ring structure of THz beam profiles can be obtained by looking at the propagation of the THz pulse originating from the dipole antenna in the time domain. The generated pulse inside the lens has been simulated using a numerical finite difference time domain (FDTD) technique backed by measurements with both sub-picosecond temporal and sub-mm spatial resolution using a fiber coupled THz detector, discussed subsequently. The top figure, 4 (a), shows the measured pulse 3.2 mm from the silicon lens. A near planar pulse front is trailed by "wings" or secondary pulse fronts delayed in time. The effect of the annular or toroidal field pattern on the lens is visible as regions of higher amplitude fields on the leading pulse front; peak amplitudes occurring 2 mm on either side of the center of the pulse structure, shown by arrows in figure 4 (a). Figure 4 (b) is the pulse measured 16 mm from the silicon lens. The same planar pulse front followed by trailing edges or "wings", is observed, a structure which is classified mathematically as a swallowtail cusp [25].

To understand the origin of this pulse shape and how it impacts the THz beam profile, it is necessary to define three regions on the silicon coupling lens corresponding to direct (*i*), marginal (*ii*), and surface wave (*iii*), contributions, shown in figure 3 (a). The direct-or paraxial-region (*i*) is defined such that rays that never cross the optical axis ($\gamma < 0$). The marginal region, (*ii*), are rays which cross the optical axis ($\gamma > 0$), but ϕ is less than critical angle in silicon. Outside of the paraxial region, marginal rays are affected by spherical aberration. Marginal rays play a large role in the THz pulse due to the dipole-surface field pattern and large Fresnel coefficients near Brewster angle. The surface wave region, labeled *iii* in figure 3 (a), is that in which the angle ϕ is beyond critical angle and incident rays experience total internal reflection. The field external to the lens is typically evanescent, but energy may be coupled to free space through surface waves due to the curved geometry of the interface [26].

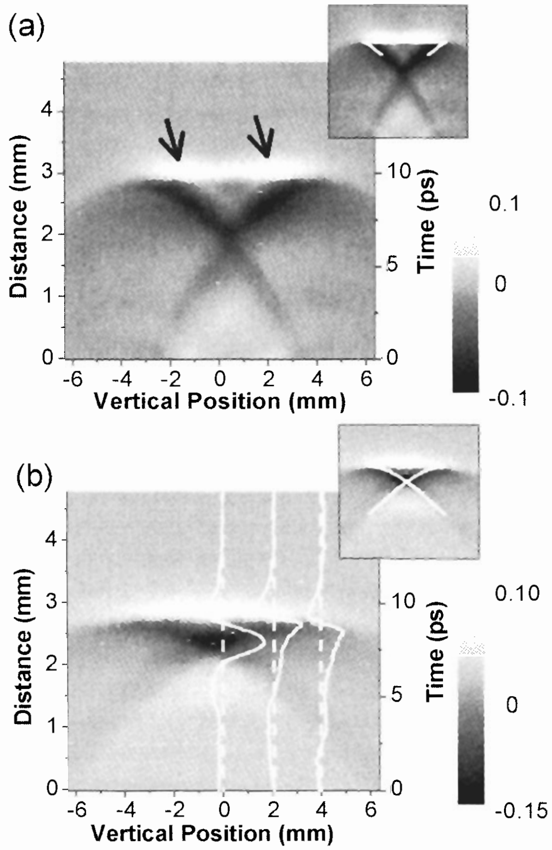

FIG. 4. Electric field measurement at $d = 3.2$ mm, (a), and 16 mm, (b), from silicon coupling lens. The arrows in (a) show relative peaks associated with annular field distribution near surface of lens. The measured pulses at positions of 0, 2, and 4 mm are overlaid on (b). Insets show an overlay of the time-of-flight model prediction.

The swallowtail pulse front arises by propagation of the pulse front along the ray paths; it is assumed the THz pulse front obeys geometrical optics. While this approach is most rigorous in the high frequency limit, such time-of-flight models can be valid for near single cycle pulses as long as the pulse is not significantly reshaped. To model propagation of the swallowtail pulse front, a stationary-phase approximation (geometrical optics limit) is used to determine the optical path length, or time-of-flight, of the pulse front to a given point in space. While the time-of-flight model is conceptually simple, it is the end result of a variational method that finds the stationary points of phase for the propagation of a given pulse front to given observation points [18]; the special case of finding the least time solutions is Fermat's principle. The observed swallowtail pulse has three stationary points which correspond to the three temporally separated pulses which make up the swallowtail pulse. The leading edge of the swallowtail THz pulse corresponds to local minima of the phase delay, while the trailing edges are local maxima.

How the pulse propagates can be seen more clearly from figure 5 (a). The rays (dashed lines) represent the paths, which correspond to real stationary values of the phase delay [18] at an undetermined point in time. The surface formed by the boundary between integer number of ray solutions forms an axial cusp caustic. Since the phase delay for any ray intersecting a caustic surface at a given point is constant, the shape of the caustic determines the pulse front surface at any given time [27]. The swallowtail pulse follows the paths of the rays shown in figure 5 (a).

Applying the time-of-flight model to the silicon lens geometry results in swallowtail pulse fronts, shown as a heavy solid line in figure 5 (a) at 90, 133, and 300 ps following optical excitation. At long times, or in the far field, the stationary points of the leading and trailing edges of the swallowtail approach the same limit, the observed spherical phase front. The insets to figures 4 (a) and 4 (b) show a comparison of the time-of-flight analysis (white line) with the measured pulses. There are several discrepancies, the time-of-flight model does not fit the observed pulse front 3.2 mm from the silicon lens. At this distance, the time of flight model, inset of figure 4 (a), shows the trailing wings of the pulse front coupled out of region *ii* are obscured by the geometric shadow of the lens surface and a swallowtail pulse should not occur. In this case, the trailing wings of the swallowtail pulse arise from radiation of surface waves [28,29] generated by the pulse front incident on the lens surface in region *iii*, beyond critical angle. The field external to the lens beyond critical angle is typically evanescent, but energy may be coupled to free space through surface waves due to the curved geometry of the interface [28]. The generation of surface waves is clearly seen in FDTD calculations, figure 5 (b). For THz frequencies (λ at 0.5 THz = 600 μm) and the 5 mm lens curvature critical angle is not uniquely defined, rather the transition between transmission and total internal reflection becomes wavelength dependent. This results in coupling into surface wave modes—especially at low frequencies—that in turn create a caustic tangent to the lens surface [26]. The propagation of these surface waves contribute to the trailing edges of the swallowtail which are not predicted by the time-of-flight model.

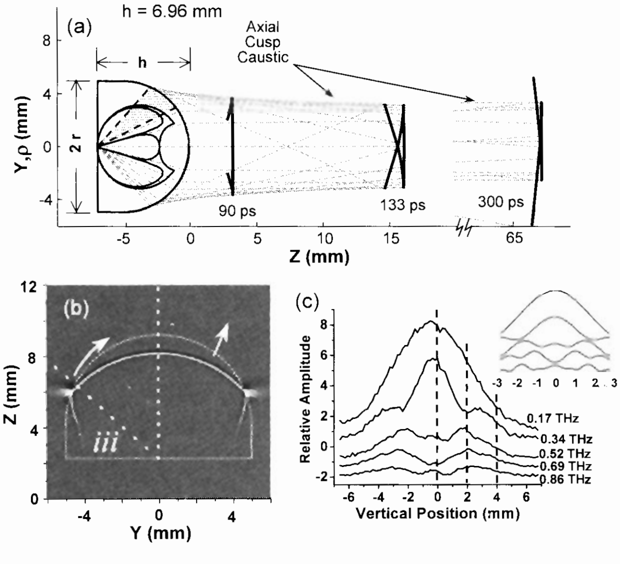

FIG. 5. (a) Time-of-flight stationary phase analysis for several propagation times/distances illustrating formation of spherical phase front at large distances for the collimating lens experimentally observed. (b) FDTD calculation of THz pulse exiting silicon lens illustrating origin of surface waves in region *iii*. (c) Spatial amplitude distribution of field measurement at d = 16 mm for five discrete frequencies. The inset shows the field distribution predicted from the time-of-flight model.

The swallowtail pulse front represents a universal behavior of wide aperture collimating lenses in the time domain, described in the most general sense by catastrophe theory [25,30]. Catastrophe theory describes the behavior of families of solutions of polynomial equations, such as those giving rise to the Seidel aberrations. An ideal lens, or real lens in the paraxial limit, produces a planar phase front from a diverging spherical wave by introducing a phase delay proportional to the square of transverse position, ρ^2. Outside the paraxial limit, as is the case here, spherical aberration introduces a quartic (ρ^4) phase correction [18]. Catastrophe theory classifies the caustic surface—the boundary between regions of space where the number of real ray solutions change—arising from such quartic dependence as an A_3 or axial cusp caustic [30]. Figure 5 (a) shows the caustic surface arising from spherical aberration [18]. Since a given point on the pulse front travels along a ray, a caustic of a given codimension will generate a pulse front—also called the travel time singularity—described by the catastrophe of the next highest codimension [27,31]. Thus, an A_3 spatial caustic (ρ^4 phase delay) will have a pulse front of form A_4 (fifth order polynomial) corresponding to the observed 'swallowtail' pulse shape in time [27,31]. Thus, an A_3 spatial caustic (ρ^4 phase delay) will have a pulse front of form A_4 (fifth order polynomial) corresponding to the observed 'swallowtail' pulse shape in time [27,31].

This swallowtail pulse shape in the time domain results, along with diffraction, in the concentric ring structure of THz beam, figure 3. Figure 5 (c) shows the spatial amplitude distribution for the spatially resolved pulse of figure 4 (b) at five frequencies within the pulse bandwidth obtained from a numerical Fourier transform of the temporal data. Individual frequencies are offset for clarity. The frequency dependent spatial amplitude distribution results from interference between the time delayed "wings" of the swallowtail and the leading edge. The mechanism giving rise to the trailing wings contributes, along with diffraction, to the previously observed [13,15,19] frequency-dependent concentric ring structure of THz beams. The inset to figure 5 (c) shows the spatially resolved amplitude distribution calculated from interference of the three pulses at any given spatial point using delays between the leading and trailing edges of the swallowtail predicted from the time-of-flight model. The calculated interference is multiplied by a Gaussian distribution with a 4.5 mm waist. For the amplitude spectra shown, the trailing edge pulse has an amplitude of 40% of the leading edge with a near π phase shift due to propagation through a caustic [18]. Although simple, the model qualitatively reproduces the amplitude distribution observed, with the exception that the calculated distributions have smaller spatial extent, probably due to the effect of diffraction.

3. THz Optical Systems

The THz beam, although exhibiting complex structure near the THz source, can be manipulated using commercially available optics to achieve efficient coupling with the THz detector. The role of the optics in the THz beam is to shape the beam if needed, and reproduce as closely as possible the beam profile generated at the THz source at the THz detector. The previous section discussed the beam profile in some detail, showing that to a first order approximation the beam behaves as a $TEM_{0,0}$ Gaussian with a 1/e amplitude waist at the output face of the silicon lens [14,15,19]. A more detailed picture of beam propagation can be obtained by considering a summation of Laguerre-Gauss modes [19]. Since the formalism of treating THz optical systems developed here applies to both fundamental and higher-order modes [21], a $TEM_{0,0}$ field distribution with a frequency independent waist diameter across the bandwidth of the THz pulse is assumed in the subsequent discussion for clarity.

The broad bandwidth THz pulse propagates out from the effective aperture of the THz source silicon lens, with each frequency component diverging due to diffraction. Assumption of a Gaussian beam profile permits a description in terms of ray matrices [21,22] to determine the beam waist (spatial field distribution) and phase front radius of curvature along the beam path. As shown in figure 2 (a), the output face of the silicon lens of the THz source is located at the focal plane of an off axis parabolic mirror. For polarization sensitive measurements it is important that any polarizers be placed after the OAPM due to cross polarization terms generated in reflection [32]. Unlike ray optics, which predicts a perfectly collimated beam, the THz beam has a second waist located one focal length from the parabolic mirror towards the target. This second beam waist has frequency dependent diameter, with higher frequencies having a smaller diameter than lower frequencies. The effect of this frequency dependent focus is to provide an effective frequency dependent aperture one focal length from the parabolic mirror. The sequence of frequency independent - frequency dependent beam waists is repeated for each confocal optic added to the system.

For most THz-TDS applications, the primary consideration of any optical system is throughput or power transfer efficiency. Losses in optical systems generally arise from losses due to absorption or scattering, losses due to reflections from optical surfaces, and losses which are due to clipping or aperturing of the beam. In addition to these loss mechanisms, power loss in THz systems also occurs due to poor overlap of beam profiles or phase front curvatures [33].

Absorption losses depend strongly on the material from which transmissive optics are made. High resistivity silicon is an ideal optical material at THz frequencies [6] exhibiting negligible loss and dispersion. Commercial optics made out of high density polyethylene are also effective, but exhibit some loss at higher frequencies. Reflective optics are metallic and have near unity reflection across the THz band. Investigations to date have used commercially available optics; due to the very long wavelengths of THz radiation compared to typical optical tolerances, an optic with a surface flatness of $\lambda/2$ across the surface at optical frequencies has a surface flatness of nearly $\lambda/1000$ at 1 THz.

Losses due to aperturing of the THz beam by optical systems can be important at low frequencies when diffraction leads to large beam diameters. A Gaussian beam going through an aperture also undergoes slight reshaping [33] which can additionally affect the throughput of an optical system. One of the major loss mechanisms for most THz optical systems is mismatch between the THz beam generated by the THz source, and, through reciprocity, the field pattern which is measured by the detector, itself a lens coupled antenna. Optimal (unity) power transfer occurs when both the beam profiles and phase front curvature overlap. It can be shown [33] that the power transfer, $C(\omega)$, for the fundamental mode as a function of frequency is given by:

$$C(\omega)=\frac{4}{\left(\frac{W_s(\omega)}{W_d(\omega)}+\frac{W_d(\omega)}{W_s(\omega)}\right)^2+\left(\frac{\omega W_s W_d}{c}\right)^2\left(1/R_d(\omega)-1/R_s(\omega)\right)^2} \tag{1}$$

where w_s is the amplitude profile 1/e radius at some point in the system of a specific mode of the beam from the source, w_d is the radius of the THz detector at the same point, and R_d and R_s are the radii of curvatures with c the speed of light in free space. More generally:

$$C(\omega)=\frac{\left|\langle\psi|\phi\rangle\right|^2}{\langle\psi|\psi\rangle\langle\phi|\phi\rangle} \tag{2}$$

Where Ψ is the Laguerre-Gauss mode from the source and ϕ is the same mode pattern of the detector.

4. THz Detectors

The THz beam is detected by an dipole antenna in conjunction with a silicon lens; a geometry that is very similar to that used for the THz source. However unlike the THz source, the detector dipole antenna is fabricated on a semiconductor with a fast carrier recombination time. Typical materials are ion-implanted silicon-on-sapphire (SOS), or low temperature grown GaAs (LT-GaAs). A typical antenna structure, figure 2 (c), is 20 μm-wide and located in the middle of a 20 mm-long coplanar transmission line consisting of two parallel 10 μm-wide lines. The spatial separation between the lines determines the frequency response of the dipole. For high bandwidth applications (100 GHz to > 5 THz) 10 μm dipoles are used. For low frequency response (< 10 GHz) and bandwidths less than 1 THz, dipole sizes can be as large as 200 μm. Since the sensitivity of the antenna is proportional to length, smaller dipoles typically have less dynamic range than that of larger antennas. A good balance between bandwidth and dynamic range is achieved with 30 μm dipoles.

The electric field of the focused incoming THz radiation induces a transient bias voltage across the 5 μm gap between the two arms of this receiving antenna. The amplitude and time dependence of this transient voltage is obtained by measuring the collected charge (average current) versus the time delay (determined by a computer controlled stepping motor with interferometric precision) between the THz pulses and the delayed Ti:sapphire laser pulses in the 5 to 10 mW detection beam. These laser pulses synchronously gate the receiver by driving the photoconductive switch defined by the 5 μm antenna gap. The detection process with gated integration can be considered as a sub-picosecond boxcar integrator. There is no observable time jitter between the THz pulses and the optical sampling pulses gating the receiver, since the same optical pulse train is used both to generate the THz radiation and to gate the receiver. The source-detector combination has polarization sensitivity of greater than 25:1 along the orientation of the dipole. This can be increased to > 200:1 (4×10^4 in power) using commercially available wire grid polarizers.

The THz receiver has been shown capable of detecting subpicosecond duration pulses coming at a 100 MHz repetition rate in a highly directional beam of THz radiation with an average power of 10 nW with signal-to-noise ratios of approximately 10,000:1 [8]. Although highly dependent on antenna geometry and the mobility of the semiconductor, a measured current of 1 nA corresponds to the electric field of an incoming instantaneous THz power level of approximately 100 μW assuming an integration time of 100, or integration bandwidth of 1.6 Hz. Consequently, the demonstrated detection limit is on the order 10^{-16} W for a signal-to-noise-ratio of unity. Because the generation and detection of the THz radiation is coherent, the THz receiver is intrinsically 1000 times more sensitive than an incoherent, liquid helium cooled bolometer.

By pre-chirping the optical excitation pulse using a grating pair and coupling it to the receiver through an optical fiber, it is possible to maintain absolute timing while being able to spatially translate the THz detector. This is useful to measure the spatial as well as temporal dependence of the electric field amplitude. To achieve sub-mm spatial resolution it is necessary to remove the collimating silicon lens on the THz detector or to use a small aperture on the lens. Both of these measures reduce the sensitivity of the detector by an order of magnitude or more and the bandwidth by approximately a factor of two. Characterization using spatio-temporally resolved THz beams is discussed in the next section.

III. CAPABILITIES OF THz-TDS

As seen in the previous section, there are several features of THz-TDS which distinguish it from better known optical characterization methods. First, in THz-TDS the electric field of the THz pulse is measured directly and phase coherently rather than the intensity envelope. The THz pulse is of extremely low power—tens of nanowatts average and less than one milliwatt peak power—so that nonlinear effects can be neglected. Since a THz pulse is near single-cycle, with a bandwidth comparable with the carrier frequency, the slowly varying envelope approximation is not applicable. Thus an accurate description of the pulse propagation requires the solution of the coupled Maxwell-Bloch equations, however since nonlinearities can, I most cases, be neglected at these low powers, materials have a linear response to the THz field. In this case linear dispersion theory can be utilized [34].

In linear dispersion theory the THz pulse is most simply represented as a superposition of plane waves of frequency ω, all with a k vector along the THz system optical axis. The relative amplitude and phase of each plane wave component of the THz pulse is obtained through a numerical Fourier transform of the measured, time resolved THz pulse electric field:

$$E(0,\omega)=\frac{1}{2\pi}\int_{-\infty}^{\infty}E(0,t)\,e^{-j(\omega t)}\partial t \tag{3}$$

Here $E(0,\omega)$ is the complex field amplitude measured at the position $z = 0$ along the optical axis. The effect of the medium through which the THz pulse propagates is described by the complex wavevector $k(\omega) = k_o(\omega) + \Delta k(\omega) - i\,\alpha(\omega)/2$ where $k_0 = \omega/c$ is the free space wave vector. $\Delta k(\omega)$ describes the frequency-dependent phase change per unit length due to both resonant and non-resonant interaction with the sample, $\alpha(\omega)$ is the power absorption coefficient. The spectral field distribution $E(z,\omega)$ for a plane-wave propagating in the z-direction through the medium at any point along the optic axis, z, can then be written as

$$E(z,\omega)=E(0,\omega)\,e^{-j(k_o(\omega)z+\Delta k(\omega)z)}e^{-(\alpha(\omega)z/2)} \tag{4}$$

By dividing equation (4) by $E(0,\omega)$ the complex wavevector, $k(\omega)$ can be directly determined. Since it is experimentally difficult to measure the pulse prior to entering the sample, the sample is typically replaced with an equivalent length of free space for which $\Delta k(\omega) = 0$ and $\alpha(\omega) = 0$. Thus two data scans are required to measure $k(\omega)$, the THz pulse transmitted through the sample (sample pulse), and the pulse after an equivalent distance of free space (reference pulse). The shape of the pulse in the time domain after propagating a distance z through a medium can be obtained from an inverse Fourier transform:

$$E(z,t)=\int_{-\infty}^{\infty}E(z,\omega)\,e^{-j(\omega t)}\partial\omega \tag{5}$$

As long as the spectral response of the medium is known, the propagation of the THz pulses through a material can derived by solving Eq. (4) or (5) which rigorously satisfy the wave equation.

One caveat to the treatment above is that with beam diameters on the order of 1 cm or less, and wavelengths which nominally range from 3 mm (100 GHz) to 100 μm (3 THz), the plane waves which comprise the THz pulse do not all propagate along the optical axis, z. Rather the THz pulse is constructed of a summation of plane waves each makes a small angle to the z axis, i.e. with small k_x and k_y components. For most THz-TDS measurements this is an unnecessary consideration since the quasi-optical system collimates and collects all the plane wave components. However as we shall see, this is not true for all measurements.

In the case consideration of the angle dependence of the plane wave basis set is important, it is accounted for by a linear plane wave expansion as above. For a given frequency, ω_o and point along the optic axis, z, the spatial distribution, $E(x,y,\omega_o)$, determines the complex amplitude of each plane wave component. Any bounded electromagnetic beam is composed of a summation of plane waves corresponding to a distribution of incidence angles [35], each with a given amplitude and phase relationship. The total k vector (momentum) of each plane wave component is given by:

$$\vec{k}=k_x x+k_y y+k_z z \tag{6}$$

with |k| conserved. The overall k vector is given by $k = \omega n(\omega)/c$ for a given frequency. The relative angle of each plane wave component with respect to the z axis is [36]: $\theta = \arctan(k_x/k_z)$, or $\phi = \arctan(k_y/k_z)$ where k_z is determined by $k_z^2 = k^2 - k_x^2 - k_y^2$. For THz-TDS case $\theta, \phi << 1$ so $\theta \cong k_x/k_z \cong k_x/k$ and similarly for ϕ. The complex amplitude of each plane wave component, $E(k_x, \omega_o)$, for a given frequency and wave vector is obtained by a second Fourier transform:

$$E(k_x,k_y,\omega_o)=\int_{-\infty}^{\infty}E(x,y,\omega_o)e^{-ik_x x}e^{-ik_y y}\partial x\partial y \tag{7}$$

The effect of this two-dimensional Fourier transform is to convert the temporally and spatially localized THz pulse into a basis set of plane waves with a given amplitude and phase relationship.

A wide variety of characterization work has been performed using THz-TDS. This includes work on gases, liquids, and a variety of material systems. Rotational states of many gas molecules fall in the THz spectral region. There has been significant work on both fundamental [37-39] and applied [40] spectroscopy, in situ spectroscopy of combustion, combustion products and high temperature water vapor [41, 42]. Since reorientation of polar molecules in liquids can be observed through at THz frequencies, THz-TDS has been used for fundamental studies on molecular dynamics in liquids [43, 44]. A wide variety of molecules have distinct signatures in this spectral range. Solid and liquid materials exhibit broad absorption bands at THz frequencies from which material properties of a wide range of samples, from polymers to semiconductors, have been determined. Using THz-TDS it is possible to perform noncontact characterization of semiconductors [45-47]. Variations of THz-TDS have been used to identify various types of DNA from low frequency vibrational resonances, distinguishing single base mutations [48, 49].

While the possible applications of THz-TDS for materials characterization are manifold, the remainder of this section will focus on a series of measurements that illustrate some of the unique measurement capabilities of THz-TDS. Here we use THz-TDS to shed some light on the question of whether or not light propagates at superluminal velocities during frustrated total internal reflection (FTIR), also known as optical tunneling [50]. While interesting from a fundamental point of view, from a practical point of view FTIR is used in fiber couplers, laser output couplers, and photon tunneling microscopes. Photonic bandgap structures are commonly used in optical devices such as vertical cavity surface emitting lasers and chirped mirrors [51]. Discussions on this subject often become heated over definitions of energy or signal velocity, and what consists of a signal; by focusing on experimental measurements, insights into optical tunneling can be gained based on rigorous and established linear dispersion theory.

The far infrared, or THz, region of the spectrum offers unique advantages for measurements of wave-packet propagation in optical tunneling. Direct measurements of the spatio-temporally resolved electric field are possible and since wavelengths range from 100 μm upwards, it is possible to accurately measure of tunneling gap dimensions. The system used to measure frustrated total internal reflection [52] consists of two matched, high resistivity silicon cylindrical wedges, 75 mm in diameter, optically polished on all faces, shown in figure 6. High resistivity silicon was used for prism materials since it has nearly negligible absorption across the THz frequency range [6] with index variations less than 0.02%, $n' = 3.4117 \pm 0.007$. The wedges have entrance and exit faces normal to the cylinder axis and inner faces with vertex angle, $\phi = 70°$. The separation between the wedges along the cylinder axis, Δ, is adjustable using a differential micrometer with a resolution of better than 1 μm. The THz pulses were P polarized with detection extinction of over 1000:1 in power, measured using a wire grid polarizer.

At critical angle, the attenuation length of the evanescent wave in the gap has a singularity, and is extremely sensitive to the angle of incidence, θ, with 20× variation over a 0.01° range [53]. As θ increases beyond θ_c, the attenuation length decreases, but also becomes much less sensitive to the angle of incidence. Since the bounded THz beam is composed of plane wave components with a range of incidence angles, the first set of measurements used the experimental system of figure 6 (a) were performed at $\beta = 0°$ corresponding to $\theta = 20°$, 3° beyond the critical angle in silicon, $\theta_c = 17.01°$. For the spatially resolved measurements discussed later, the system was modified as shown in figure 6 (b) with the wedges tilted to $\beta = 10°$ to achieve an angle of incidence on the interior wedge face of $\theta = 17.1°$.

For optical tunneling measurements the reference pulse, $E_R(t)$, is the pulse measured for no separation of the wedges, $\Delta = 0$ μm. Measurements of the transmitted sample pulse, $E_T(t)$, were made for $\Delta = 100$, 200, 500, and 1000 μm. These measurements are shown as points in figure 7 and show pulses arriving earlier in time with strong attenuation and pulse reshaping as Δ increases. For clarity and to emphasize the pulse reshaping, pulses for each value of Δ have been plotted on separate vertical scales. The reference amplitude spectrum, $E_R(\omega, \Delta=0)$, obtained from a numerical Fourier transform of the time domain data, is shown as points in figure 8 (a) with the associated spectra at different gap widths, $E_T(\omega)$. The amplitude spectra have not been scaled, the area under each curve squared is proportional to the transmitted pulse energy.

The theoretical transmission through the wedge system shown in figure 6 can be determined by adapting the well known result for transmission through a dielectric slab [18]:

$$E_T(\omega) = \frac{t_{01} t_{10} e^{i\beta}}{(1 - r_{01} r_{10} e^{i2\beta})} E_I(\omega) \tag{8}$$

The dielectric slab is of thickness, d, and the radiation is incident at angle θ_0. The Fresnel coefficients are t_{01}, t_{10}, r_{01}, and r_{10} for transmission and reflection at the n_0-n_1 and n_1-n_0 boundaries respectively. $\beta = n_1 k_o d \cos\theta_1$ is the phase delay associated with multiple reflections inside the slab. θ_1 is the angle of the transmitted radiation inside the slab determined from Snell's law, $n_0 \sin\theta_1 = n_1 \sin\theta_1$. This formula is modified to account for the wedge geometry [54]:

$$E_T(\omega) = E_T(\omega) = \frac{t_{01} t_{10} e^{i\beta} e^{i\gamma}}{(1 - r_{10} r_{01} e^{i2\beta})} \times e^{i\Phi} \times E_o(\omega) = H(\omega) E_o(\omega) \tag{9}$$

with $\gamma = k_o n_0 d \cos\theta_0$ and $\Phi = n_1 k_o \Delta - n_0 k_o \Delta$, assuming normal incidence. Applying equation (9) to the measured reference field, $E_O(w)$, the calculated THz pulse transmitted through the cylindrical wedges is obtained by taking an inverse Fourier transform of the

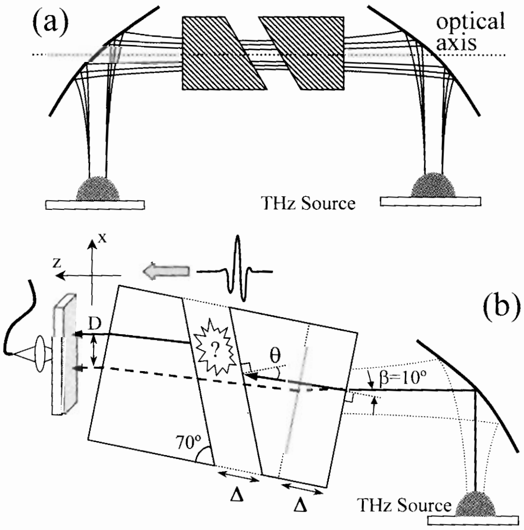

FIG. 6. (a) THz time-domain spectroscopy system used for measuring frustrated total internal reflection. The THz beam propagates along the indicated optical axis. (b) Experimental schematic using fiber coupled THz receiver. Dashed line represents propagation path for $\Delta = 0$ μm, while solid line is for $\Delta = 1000$ μm.

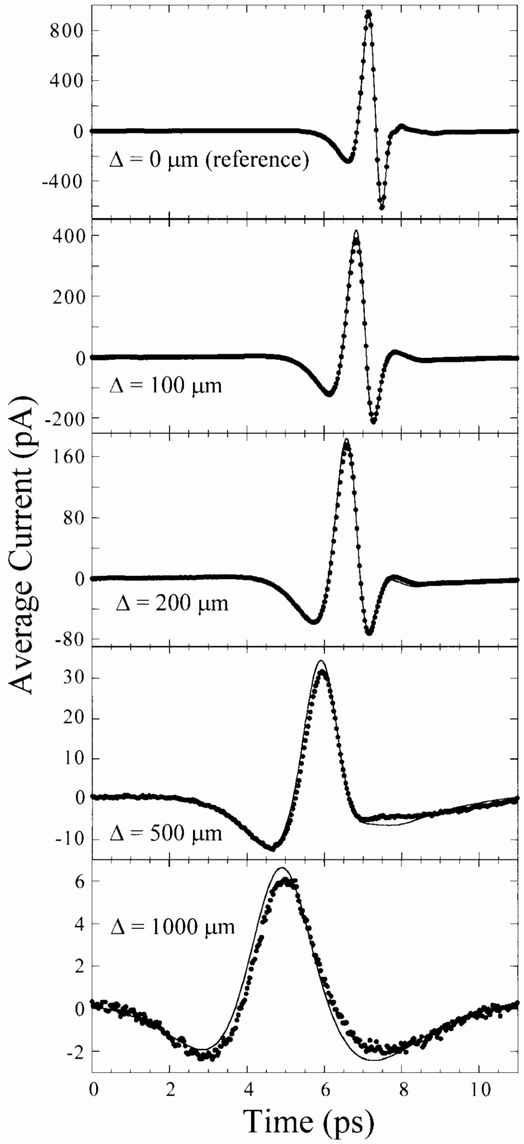

FIG. 7. Measured THz pulses (points) propagating through FTIR cylindrical wedges with Δ= 0, 100, 200, 500 and 1000 μm. The linear dispersion theory fit is given by the solid line.

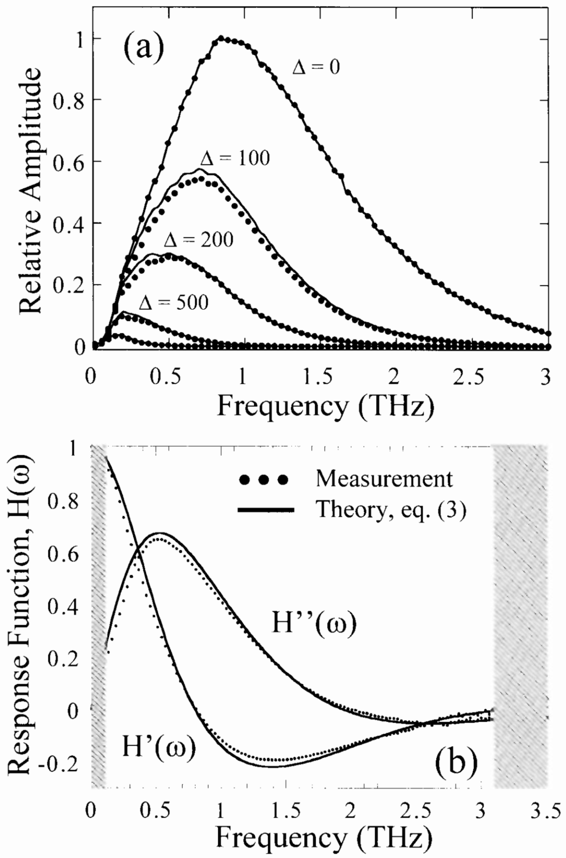

FIG. 8. (a) Measured amplitude spectra (points) corresponding to the THz pulses of figure 7 with theoretical predictions (lines). The amplitude spectra are presented as measured with no scaling. (b) The measured real and imaginary parts of the system response Re{H(ω)} and Im{H(ω)}, points, and fit using the linear dispersion theory (solid line) of equation (9).

complex amplitude $E_T(\omega)$. The calculated THz pulse is plotted as a solid line on top of the data for Δ = 100, 200, 500, and 1000 mm in figure 2 (a). The calculated amplitude spectra, again given as solid lines, are overlaid on the experimental measurements in figure 2 (b). Agreement is excellent with no floating parameters, indicating the model of equation (9) accurately describes the measured amplitude and phase changes of a THz pulse undergoing frustrated total internal reflection.

Although this analysis based on linear dispersion theory is in good agreement with measurement, it does not answer the question of superluminal propagation. This is because there is a fundamental uncertainty in the path the pulse propagates through this system; one reason it has been difficult to assign a characteristic time for optical tunneling [50]. However the fact that this is a linear system permits us to define $H(\omega)$ as the complex frequency domain system response function, $H(\omega) = H'(\omega) + iH''(\omega) = E_T(\omega, \Delta)/E_O(\omega, \Delta{=}0)$. The ability of THz-TDS to directly determine $H(\omega)$ over the range from 100 GHz to over 3 THz, limited only by the system bandwidth. Figure 8 (b) shows measured values of $H'(\omega)$ and $H''(\omega)$ as points for Δ = 100 μm. The calculated values of $H(\omega)$ from equation (9) are overlaid as a solid line. The measurement of $H(\omega)$ can be used to determine causality in optical tunneling since in any causal system the real and imaginary part of $H(\omega)$ are related through the Kramers-Kronig relations [55]. Although noise on the data for frequencies below 100 GHz and above 3 THz precluded using the measured values of $H(\omega)$ to directly verify causality, the Kramers-Kronig integral was determined over the frequency range 0 to 20 THz for equation (9). The real and imaginary components determined through the Kramers-Kronig relationships are given as a dashed line in figure 8 (b). Thus THz-TDS shows causal propagation in optical tunneling based upon agreement of the measured pulse with a simple model based on linear dispersion theory which makes no assumptions of optical path, and contains no floating parameters.

Temporal pulse reshaping makes it impossible to assign a time to pulse tunneling [56]. However by using the fiber coupled THz detector system described previously, it is possible to observe both the temporal and spatial reshaping of pulses after undergoing optical tunneling, enabling direct measurement of the phase and amplitude shifts of the plane waves which form the THz pulse's basis set.

For these measurements the time resolved THz field was measured using a fiber coupled THz detector with a resolution of 1 mm orthogonal to the THz beam—x direction in figure 6 (b)—to obtain the electric field E(x,t) [57]. Contour plots of the normalized time resolved beam profiles are shown in figure 9 for the reference pulse with $\Delta = 0$, and the pulse which has tunneled through an optical barrier of width $\Delta = 1000$ μm, $E_F(x,t)$. Comparing the two measured profiles, $E_F(x,t)$ shows an apparent shift of -1.79 ps relative to $E_o(x,t)$ and a lateral shift of 2.8 mm in the positive x direction. The path of the pulse is opposite of that assumed in previous studies of a THz pulse undergoing optical tunneling [52]. From these spatial measurements it is clear why the pulse appears to arrive earlier in time, the transmitted pulse for $\Delta \neq 0$ propagates through less high index material than the pulse with $\Delta = 0$. The spatial shift arises from the Goos-Hanchen shift that occurs during total internal reflection of a spatially bounded beam [36,53,58].

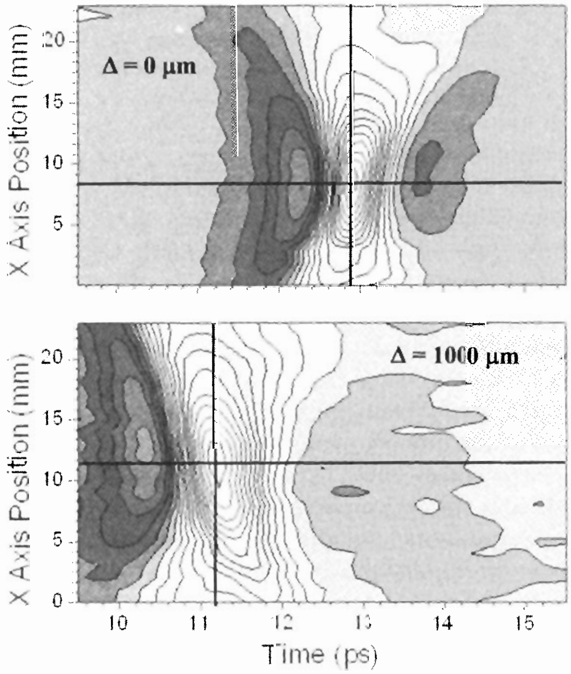

FIG. 9. Contour plots of $E_o(x,t)$ at $\Delta = 0$ μm with 15 pA contour spacing and $E_T(x,t)$ at $\Delta = 1000$ μm with 5 pA spacing illustrating temporal and spatial shift of THz pulse.

Similar to the way in which temporal pulse reshaping makes it impossible to assign a time to pulse tunneling [56], spatial pulse reshaping makes it difficult to assign a well defined path to spatially localized wave packets. However by using equation (7) it is possible to convert the measured pulse into a basis set of plane waves each traveling at some angle ϕ to the optic axis. The two dimensional Fourier transform of the reference, $\Delta =$ 0 μm, and sample $\Delta = 1000$ μm, pulses are shown in figure 10. Comparing these two measurements, the peak spectral component of $|E_F(k_x, \omega)|$ has shifted from 0.32 THz to 0.21 THz due to attenuation of the high frequencies in the barrier. The amplitude spectrum also is reshaped, or filtered, along the ϕ axis due to the rapid increase of the amplitude attenuation length as the incident plane waves approach critical angle; negative values of ϕ correspond to an increase in the incidence angle on the barrier. This wave vector filtering results in a change in propagation direction for the overall pulse as observed previously at optical frequencies [59].

By breaking the pulse which propagates through the optical tunneling barrier into its component plane waves it is possible to extract the phase and loss times associated with propagation through the silicon wedge system. The system is defined by the complex transfer function $H(k_x, \omega)$:

$$\frac{E_F(k_x,\omega)}{E_o(k_x,\omega)} = H(k_x,\omega) = |H(k_x,\omega)|e^{i\phi(k_x,\omega)} \tag{10}$$

The magnitude of the complex transfer function, $|H(k_x, \omega)|$, is shown in figure 10 (c) and shows three distinct regimes: low signal region, thick barrier limit and thin barrier limit. Regions where $E_o(k_x,w)$ has near zero amplitude, low signal region, have been removed from this plot. The thick barrier limit is where the transfer function has near zero value and the transfer function is dominated by the exponentially decreasing amplitude, $|H| << 1$. The thin barrier limit has small amplitude attenuation and the transfer function is dominated by the phase term, $e^{i\phi(\omega,kx)}$ and these plane wave components are preferentially transmitted. The dotted line in figure 10 (c) indicating boundary between the thick and thin barrier regions is a guide to the eye.

The transfer function contains a complete description of pulse propagation through the wedge-gap system. A complex traversal time, $\tau_c = \tau_\phi + i\,\tau_L$ can be defined for propagation of the THz pulse through the wedge/

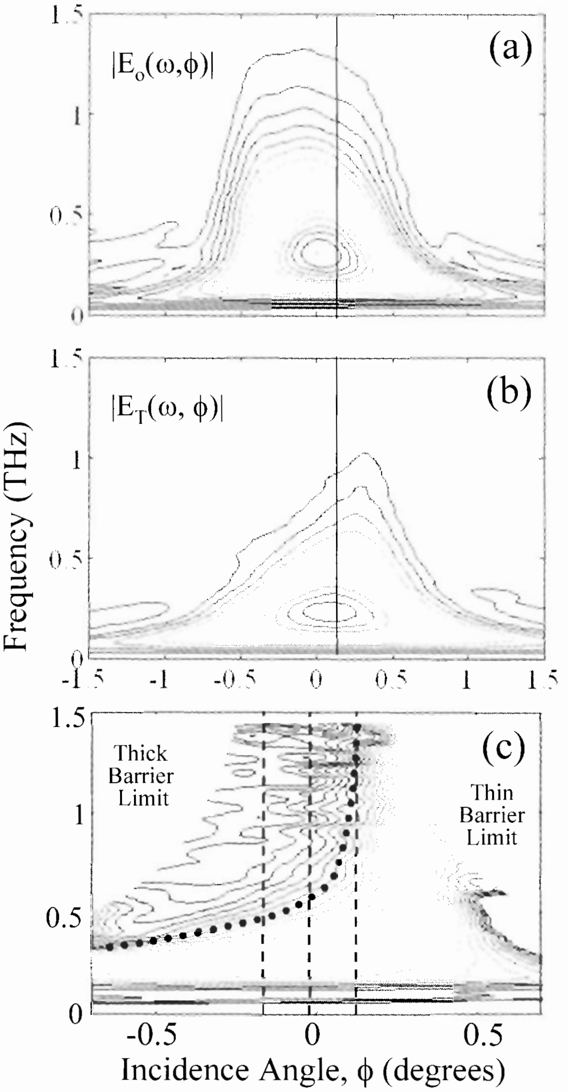

FIG. 10. (a) Reference pulse spectrum, $|E_o(\phi,\omega)|$, $\varDelta = 0$ μm. (b) Sample pulse spectrum, $|E_T(\phi,\omega)|$, $\varDelta = 1000$ μm normalized to $|E_o(\phi,\omega)|$. Contour line spacing is 0.05 and vertical line represents critical angle, θ_c. (c) System transfer function, $|H(\phi,\omega)|$. Dashed lines are constant ϕ values shown in figure 11, and dotted line represents thick and thin barrier boundary.

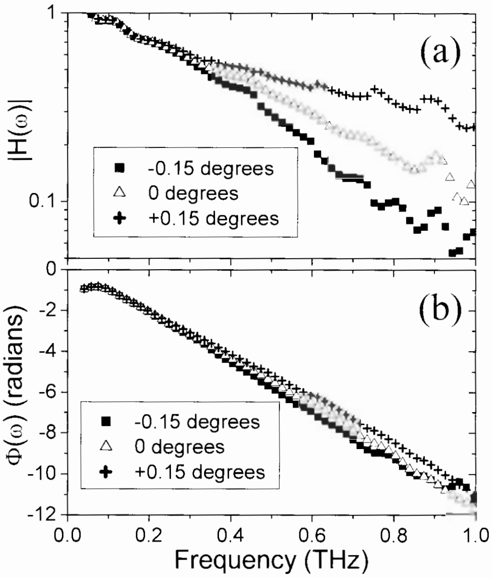

FIg. 11. (a) Semilog plot of $|H(\phi,\omega)|$, (b) phase, $\Phi(\phi,\omega)$ for ϕ = -0.15°, 0°, +0.15°. Line slopes give loss and phase times respectively.

gap system [59,60]. The complex traversal time is given by the phase time τ_ϕ (also called the net group delay) and a loss time, τ_L. The phase time corresponds to the group velocity, while the interpretation of the loss time is the shift of the pulse earlier in time due to the pulse reshaping [61].

$$\tau_\phi = \frac{\partial\phi}{\partial\omega}; \quad \tau_L = -\frac{\partial \ln|H(k_x,\omega)|}{\partial\omega} \tag{11}$$

The amplitude and phase of $H(k_x,\omega)$ as a function of frequency is shown for three different values of ϕ are shown in figure 11; the corresponding phase and loss times are given by the slopes of the lines. The loss time depends strongly on the incident angle of a given plane wave component, τ_L = 1.4 ps, 2.4 ps, and 3.4 ps for ϕ = -0.15°, 0°, and +0.15° respectively. The change in values of the loss time with angle of incidence shown that frequency dependent pulse reshaping is a strong function of the angle of incidence. The phase times are τ_ϕ = -1.25, -1.18, -1.06 ± 0.15 ps for ϕ = -0.15°, 0°, and +0.15°, on the same order as the measured peak shift of -1.79 ps in figure 9. The phase times obtained from figure 11 are negative, corresponding to a shift forward in time. These loss and phase times are analogous to those measured previously by measuring beam angle divergence with CW optical frequencies [59], but are determined directly from phase coherent data over a broad spectral range. However for the 1 mm gap and frequency spectrum measured here, we do not observe saturation of the phase times.

To conclude this section on THz materials characterization we have used frustrated total internal reflection, or optical tunneling, and a microcosm of how THz-TDS can be used to measure fundamental material properties. By direct measurement of the electric filed it is possible to measure both the real and imaginary, or magnitude and phase, of any system response function. Typically this would correspond to the absorption and index of the material being investigated. However as shown above, this can also correspond to the complex transfer function of the system or to phase and loss times. While the time domain measurements of optical tunneling show the arrival of a pulses' peak comes earlier in time as the tunneling barrier width increases, the broad bandwidth and high dynamic range of

THz-TDS show this is due to strong spectral reshaping, figure 8. Via the fact that THz-TDS is phase coherent, allowing measurement of both the real and imaginary parts of the system transfer function, optical tunneling is shown to be causal. Finally by spatially and temporally resolving the electric field the transmission for each plane wave component is measured, demonstrating the incidence angle dependent of optical tunneling. From these measurements it is clear that the lateral shift of a pulse due to the Goos-Haanchen phase shift is why the pulse seemingly travels superluminally: it is traveling through less high index material.

IV. APPLICATIONS OF THz-TDS

It was once said that all of ultrafast optics was a tool looking for an application, although such statements are no longer voiced since ultrafast has begun to find niche applications in materials processing. The same statement may certainly apply to THz-TDS for non-scientific measurements; no application has emerged in which THz-TDS is the most effective characterization tool. Here "effective" means that the need for results of a particular accuracy justify the cost and complexity of the technique. Some of this may be due to the fact that the capabilities of THz-TDS, while growing, are not widely known outside the scientific community. Following the format used throughout this review article, this section will discuss briefly two potential applications of THz-TDS: measurement of thin films and non-destructive evaluation of ceramic bearings.

1. THz Interferometry

Characterization of materials has been one of the enabling roles of optics in modern day industry. Interferometers and spectrometers are often used to characterize thin films; the accurate measurement and control of film thickness is critical to applications from semiconductor processing to food packaging [62]. While techniques such as variable angle spectroscopic ellipsometry and phase-contrast microscopy are widespread, they are not applicable for measurement of opaque films. Here THz-TDS and THz tomography [63] may find a niche in characterizing thin films which are opaque in the visible and near infrared regions of the spectrum.

Measuring thin films, which cause small perturbations on a broad bandwidth spectrum, presents a challenge since THz wavelengths are typically mm to sub-mm. When $k(\omega)d \ll 1$, with $k(\omega)$ the complex, frequency dependent wave constant and d the sample thickness, noise or changes between the sample and reference pulse lead to errors which are greater than the small changes being measured. One way to separate these small changes is to induce a modulation on the beam by the sample. This technique has been pursued with great success by the group of X.-C. Zhang at Rensselaer Polytechnic Institute through use of differential time domain spectroscopy (DTDS). DTDS dithers the sample in and out of the THz beam using a shaker or galvanometer and has been used to determine the refractive index of a 300 nm-thick parylene-N film and other thin or low index materials [64-66]. By using a double modulation technique in which both the sample and the THz beam itself are modulated and measured using two lock-in amplifiers [67] films as thin as 100 nm have been characterized.

An alternative technique is THz interferometry [68,69] which splits the THz pulse train into two equal parts, providing a near π, frequency independent phase shift to one of the parts. In this case destructive interference occurs, eliminating the background signal, drift, and some noise sources. This is accomplished via a Michelson interferometer, as shown in figure 12, although it is possible to also use other configurations, such as a Mach-Zender interferometer. The near π phase shift can be achieved from a Gouy phase shift [69], total internal reflection [68], or geometrical rotation of the electric field vector with a roof mirror as shown in the figure. The π phase shift of a beam passing through focus, Gouy shift, depends on the distance from the focus, and is π only at very long distances. While phase shifts occur on total internal reflection, they

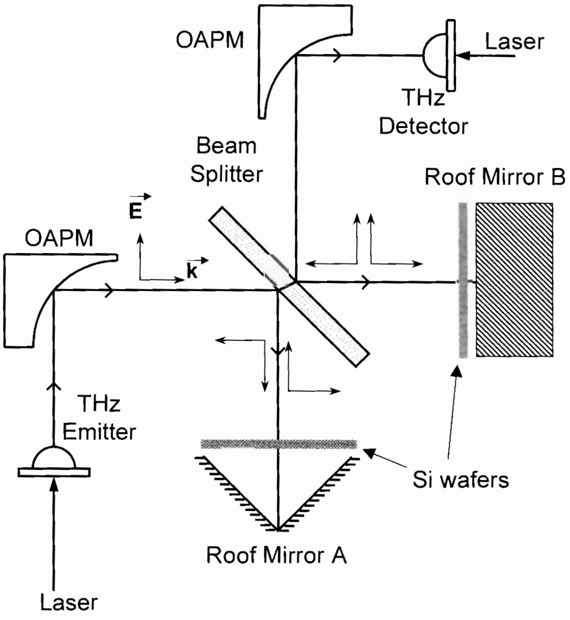

FIG. 12. Diagram of THz interferometer. The beam splitter is high resistivity silicon and roof mirrors are first surface aluminum. The silicon wafers in arms A is illuminated at Brewster angle using a HeNe to induce the measured index change.

approach p only in the limit of incident angle near 90° or an infinite index of refraction. Geometrical field vector rotations are the most effective, however they require the THz beam to have rotational symmetry, section II, to achieve a π phase shift.

In THz interferometry the signal measured by the THz detector is a superposition of the signal from the reference and sample arms:

$$E_{meas}(\omega)=E_{ref}(\omega)+E_{samp}(\omega) \tag{12}$$

The signal from the sample arm contains the modulation of the THz pulse by the sample. If the $k(\omega)d << 1$ and secondary reflections can be ignored:

$$E_{meas}(\omega)=E_{ref}(\omega)\left[1-\exp(-ik_o(n(\omega)-1)d+i\Phi(\omega))\right] \tag{13}$$

where the phase error term, $\Phi(\omega)$, accounts for any effect which contributes to incomplete destructive interference, and is determined experimentally by taking a scan with no sample in the interferometer. By expanding the exponential in equation (13) in a series:

$$\frac{E_{meas}(\omega)}{E_{ref}(\omega)} \cong k_o n_i(\omega)d+ik_o\left[n_r(\omega)-1\right]d+i\Phi(\omega) \tag{14}$$

In the case that $k_o(n(\omega)-1)d$ is not much less than one, or in the case that the Fabry-Perot oscillations of the samples are not negligible, is not possible to determine an analytic solution for the frequency dependent complex index. However the index can be extracted numerically by using a Nelder-Mead downhill simplex algorithm.

THz interferometry has several advantages over THz-TDS for thin film measurement. First, it is less sensitive to long term fluctuations in the THz signal than standard THz-TDS. Expressing the drift between the sample and reference spectra by a small drift error term, $\Delta(\omega)$, such that $\exp(i\Delta(\omega)) \cong 1$ and adding the drift term,

$$\frac{E_{meas}(\omega)e^{i\Delta(\omega)}}{E_{ref}(\omega)} \cong 1+i\left(\Delta(\omega)-\frac{\omega}{c}(n_r(\omega)-in_i(\omega)-1)d\right) \tag{15}$$

for standard THz-TDS. From this it is seen that drift errors are additive to THz-TDS measurements. For interferometric measurements, the error can be found by including the drift error term in equation (14):

$$\frac{E_{meas}(\omega)e^{i\Delta(\omega)}}{E_{ref}(\omega)} \cong \left[1+\Delta(\omega)\right]\left\{k_o n_i(\omega)d+ik_o[n_r(\omega)-1]d+i\Phi(\omega)\right\} \tag{16}$$

showing the drift error term is multiplicative with the measured values of the complex index. For typical values of thin films ($d \cong 1$ μm, $n_r \cong 2$, $\Delta \cong 1\%$) the increase in measurement accuracy is on the order of a factor of 50.

THz interferometry is also less susceptible to some sources of experimental noise, leading to more accurate measurements for thin films. In THz-TDS the transmission coefficient is determined from the ratio between sample and reference scans with magnitude (modulus) $\rho(\omega)$, and phase term (argument) $\varphi(\omega)$. The real part of the complex refractive index, $n(\omega) = n'(\omega) - in''(\omega)$, is extracted from the argument, $\varphi(\omega)$, and the absorption coefficient from the modulus, $\rho(\omega)$. Errors in the measurement of $n(\omega)$ can be shown [70] to be proportional to the variance of the modulus, $\sigma_\rho^2(\omega)$. In the case $\rho(\omega)$ approaches unity, i.e. $k(\omega)d << 1$, $\sigma_\rho^2(\omega)$ is simply proportional to the variance of the noise divided by the spectral amplitude of the reference pulse. The noise contributions arise from three sources [70]:

$$\sigma^2_{noise}(\omega)=\rho^2(\omega)\sigma^2_e(\omega)+\sigma^2_{sh}(\omega)+\sigma^2_d(\omega) \tag{17}$$

where $\rho(\omega) \cong 1$. These three terms correspond to the THz emitter $\sigma^2_e(\omega)$, shot noise in the THz detector $\sigma^2_{sh}(\omega)$, and other signal independent noise sources, $\sigma^2_d(\omega)$ such as laser noise, electronic noise, and Johnson noise [8,70]. The shot noise can be written as $\sigma^2_{sh}(\omega) = 2e\Delta fX(\omega)$ with e the electron charge, Δf the measurement bandwidth determined by the lockin integration time, and $X(\omega)$ either $R(\omega)$ or $S(\omega)$. As shown in reference [70], the dominant noise term comes from the THz emitter, $\sigma^2_e(\omega)$, especially in the case of slightly absorbing samples with $\rho(\omega)$ approaching unity, and $S(\omega) \cong R(\omega)$.

For THz-TDS the sample and reference scans are measured independently and the noise on the sample and reference scans are uncorrelated. However for THz interferometry, a more relevant noise figure is given by the variance of the measured interference signal, $D(\omega) = R(\omega) - S(\omega)$. Since in THz interferometry the difference is obtained in a single measurement, the emitter noise is correlated and the noise on the interferometric signal can thus be written:

$$\sigma^2_{int}(\omega)=(1-\rho(\omega))^2\sigma^2_e(\omega)+2e\Delta fR(\omega)(1-\rho(\omega))+2\sigma^2_d(\omega) \tag{18}$$

Comparison of (17) with (18) shows that the effects of both the shot noise and emitter noise are substantially reduced in THz interferometry.

The final advantage of THz interferometry for measuring thin films is sensitivity to subwavelength changes in optical path since the THz interferometer acts as a phase coherent white light interferometer. The film thickness resolution is less than the Sparrow criterion [71] which states that two pulses are resolvable if there is a minima between their peaks. In measuring the superposition of two pulses of opposite sign, when one pulse is time shifted relative to the other by an amount large enough that the summation of the pulses is above the signal to noise ratio of the system, a signal is measurable. The measurable time shift is determined by the time rate of change of the measured electric field, $\partial/\partial t\ E(t)$. For typical interferometer data, the measured electric field has a slope of approximately 200pA/ps. With the minimum detectable signal on the order of 0.2 pA, this corresponds to a time resolution of 1 fs or the ability to detect films of thickness on the order of 100 nm. THz systems with higher bandwidth have correspondingly better sensitivity.

To demonstrate how THz interferometry can be used for optical characterization, the index of refraction of high resistivity, > 10 kΩ-cm a silicon wafer is modified through optical excitation. In this case the frequency dependent change in refractive index, $\Delta n(\omega)=\sqrt{\varepsilon_r(\omega)}$, can be described by the Drude model [72]:

$$\varepsilon_r(\omega)=\varepsilon_\infty-\sum_{j=e,h}\frac{\omega_p^2}{\omega(\omega+i\Gamma_j)} \tag{19}$$

where ε_∞ = 11.7 is the relative permittivity of Si, ω_p is the electron or hole plasma frequency given by $\omega_p^2 = Ne^2/\varepsilon_0 m_{e,h}^*$ with free-space permittivity ε_0, carrier density N assumed equal for electrons and holes, and effective masses m_e^* = 0.26 and m_h^* = 0.37 [45]. Γ_j is the carrier damping rate $1/\tau_{e,h}$. Using an excitation intensity of 36 μW/cm^2 results in a uniform carrier density of N = 6.53×10^{12} cm^{-3}.

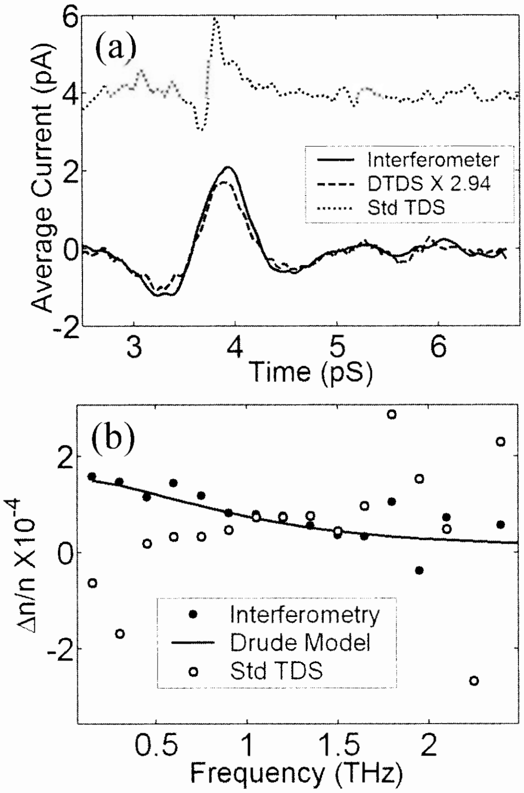

FIG. 13. (a) THz pulses measured using THz interferometer (solid line), DTDS (dashed line), and the difference between two consecutive THz scans taken with and without optical excitation (dotted line). (b) Optically induced change in refractive index determined from THz interferometry (dots), THz-TDS (open circles), and Drude theory (line).

Figure 13 (a) compares the difference between two consecutive THz scans taken with and without optical excitation (dotted line), a single data scan on the THz interferometer (solid line), and a scan taken using DTDS (dashed line). For the interferometer scan the background, $\Phi(t)$, was subtracted. The DTDS scan has been normalized to the throughput of the THz interferometer. This comparison shows the noise improvement of THz interferometry and sample modulation techniques such as DTDS for optically thin samples. These differences are more apparent when extracting the optically induced change in refractive index, $\Delta n(\omega)/n$, obtained from THz interferogram (points) and that determined by THz-TDS (open circles). The index change calculated using the calculated from Drude theory, equation (19), is shown as a solid line. From this it is seen that THz interferometry offers a sensitive tool for characterization of thin films. Index changes of < 10^{-4} can be measured, corresponding to a change in optical path length of 342 nm. At 0.7 THz, the peak of the THz amplitude spectrum, this is an optical path length change of λ/1250. Extrapolating the results to a unity signal to noise ratio, the measurement limit of the system is 32 nm or λ/13,500.

2. Non-Destructive Evaluation

Previously THz-TDS has been extensively used for electromagnetic scattering measurements as a potentially simple way to identify complex targets by the late time response [73,74]. The sub-picosecond temporal resolution permits accurate time gated measurements for fundamental investigations of scattering mechanisms and has enabled the first direct experimental observations of fundamental surface wave velocities, loss mechanisms [75], and Gouy phase shifts [76]. Many of the dielectric materials characterized by this technique have been ceramics, which can be highly transparent in the THz spectral region. Since the THz electromagnetic scattering signature is highly dependent on the path the radiation takes through a given target, THz-TDS can be used for detecting fractures in materials which are opaque to visible radiation but transparent to THz, such as ceramic bearings.

Ceramic materials find multiple uses such as turbine blades, ball bearings, heat components, ballistic armor, and grinding media, because they can withstand high temperatures and stress. Due to their hardness, wear resistance, and the ability to finish them to high tolerances one of the most common uses of ceramics is ball bearings. Ball bearings are formed by casting and firing, rough grinding, then lapping to high tolerance and surface finish. In the grinding process bearing can undergo high stress thus resulting in both surface and subsurface cracks. A variety of techniques are used to detect fractures in ceramic materials including optical microscopy, dye impregnation, acoustic emission, and acoustic microscopy.

The THz experimental system used for nondestructive evaluation is similar to those used in previous investigations of electromagnetic scattering [74], but a fiber coupled detector is used, figure 14. Alumina (amorphous Al_2O_3) ball bearings with diameters of ¼" and ⅜" respectively were fractured by means of thermal shock, producing scale-like cracks. Spheres exhibit three main scattering mechanisms: specular, back axial, and surface waves, indicated in figure 15 [73]. The surface wave travels around the circumference and also cuts through material at acute bistatic observation angles. These pulses are shown in figure 15 (a) for an alumina bearing with no fractures. These three scattering mechanisms are each affected differently by fractures internal to a damaged bearing. Fractures in the bearing act like scattering centers reshaping the pulse and leading to additional structure, which is visible in figure 15 (a). The first pulse, corresponding to the specular reflection, encounters no scattering points, and there is little change in the pulse shape. The surface and back-axial reflections, however, display large discontinuities between the reference and fractured bearings. Changes to the spectrum are highlighted in the lower trace, which shows the difference between the damaged and undamaged bearings.

While analysis of backscattering from ceramic bearings can indicate the presence of cracks, it takes approximately ten minutes to acquire the traces shown in figure 15 (a). Combining scattering with sample modulation allows much faster determination of bearing integrity. A uniform sphere has complete rotational symmetry, which is broken if the spherical bearing has defects or fractures. It is possible to utilize this property of symmetry to be able to make a rapid determination of whether fractures exist in ceramic bearings by rotating the bearing at a constant angular velocity, ω, and, using a lock-in amplifier, to detect scattered or transmitted THz radiation modulated at ω. Fractures in the rotating sphere modulate the THz pulse; each fracture point acts as a periodic scattering center determined by the rotation of the target. For this measurement the THz pulse transmitted through the

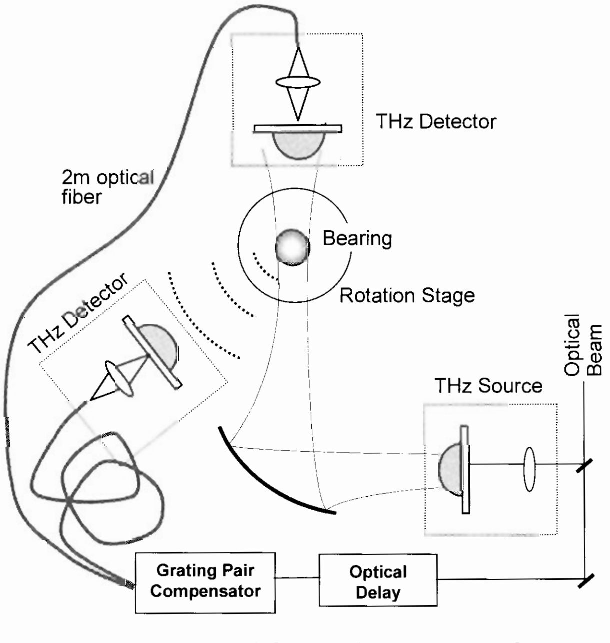

FIG. 14. System used for nondestructive evaluation of alumina bearings. The fiber coupled THz detector is used at the positions shown for forward or backscattering measurements. The alumina bearing can be rotated at up to 35 Hz.

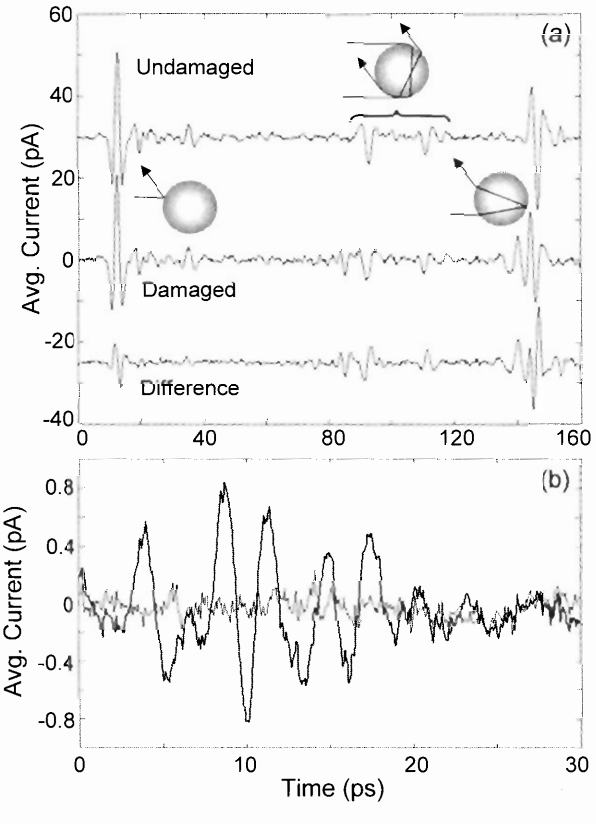

FIG. 15. (a) Measured back scattered signal from undamaged and damaged bearings. The undamaged scan has been offset by 30 pA for clarity. The lower scan, offset -15 pA is the difference. Insets illustrate specular, surface, and back axial reflections. (b) Forward scattering signature of 10th harmonic of angularly modulated bearing. The heavy line is the damaged bearing while the light line is the signal from the undamaged bearing.

alumina bearing (forward scattering) was measured, and is shown in figure 15 (b). To minimize noise the tenth harmonic of the rotational frequency was measured. A clear difference is observable between the forward scattered signatures. Similar results can be obtained using backscattering, but eccentricities in bearing rotation of approximately 70 μm make it more difficult to determine whether the signal is due to fractures.

V. SUMMARY AND CONCLUSIONS

This brief review has covered the characterization technique of THz time domain spectroscopy in terms of creating and detecting broad bandwidth THz beams, examples of how it can uniquely determine material properties, and applications in characterization of thin films and non-destructive evaluation. Rather than provide an overview of recent results a few applications were discussed in depth. THz-TDS has been used for a wide range of measurements and a large number of articles.

Similarly the discussion here has focused on broadband generation using photoconductive switches. As alluded to in the introduction, this merely a small subset of the host of techniques which allow both CW and pulsed THz generation and measurement. The most similar technique to that discussed here has been pioneered by X. C. Zhang's group. Results similar to those presented here have been obtained using difference frequency generation and the electro-optic effect to generate and detect THz pulses with bandwidths to beyond 30 THz. Reviews of time domain THz techniques as well as forays into THz from the optical and electronic regimes can be found in references [2,77-85].

The work reviewed in this paper was presented at IPTC 2003 in Seoul, Korea. The author wishes to acknowledge the hospitality of both the Optical Society of Korea and the people of Korea. The work discussed includes contributions by a large number of individuals, particularly D. Grischkowsky, M. T. Reiten, S. A. Harmon, J. Small, S. Krishnamurthy, and L. Hess. The author would like to acknowledge support from the National Science Foundation (ECS-9984896), Army Research Office (DAAD19-99-R-BAA8), and Department of Energy.

* Corresponding author : kridnix@okstate.edu

REFERENCES

[1] Committee on Optical Science and Engineering, *Harnessing light: Optical science and engineering in the 21st century.* Washington, D. C.: National Academy Press, 1998.

[2] P. D. Coleman, "Reminiscences on selected millennium highlights in the quest for tunable terahertz-submillimeter wave oscillators," *IEEE J. Quantum Electron.*, vol. 6, pp. 1000-1007, 2000.

[3] C. M. Snowden and D. P. Steenson, "Circuits and simulations at 1 THz," *Phil Trans. R. Soc. Lond. A*, vol. 354, pp. 2435-2446, 1996.

[4] C. Fattinger and D. Grischkowsky, "Point source terahertz optics," *Appl. Phys. Lett.*, vol. 53, pp. 1480-2, 1988.

[5] C. Fattinger and D. Grischkowsky, "Terahertz beams," *Appl. Phys. Lett.*, vol. 54, pp. 490-2, 1989.

[6] D. Grischkowsky, S. Keiding, M. van Exter, and C. Fattinger, "Far-infrared time-domain spectroscopy with terahertz beams of dielectrics and semiconductors," *J. Opt. Soc. Am. B*, vol. 7, pp. 2006-15, 1990.

[7] M. van Exter, C. Fattinger, and G. Grischkowsky, "High-brightness terahertz beams characterized with an ultrafast detector," *Appl. Phys. Lett.*, vol. 55, pp. 337-339, 1989.

[8] M. van Exter and D. R. Grischkowsky, "Characterization of an optoelectronic terahertz beam system," *IEEE Trans. Microwave Theory Tech.*, vol. 38, pp. 1684-91, 1990.

[9] P. Goldsmith, *Quasioptical Systems.* (Piscataway, NJ: IEEE Press, 1998.)

[10] S. E. Ralph and D. Grischkowsky, "Trap-enhanced electric fields in semi-insulators: the role of electrical and optical carrier injection," *Appl. Phys. Lett.*, vol. 59, pp. 1972-4, 1991.

[11] N. Katzenellenbogen and D. Grischkowsky, "Efficient generation of 380 fs pulses of THz radiation by ultrafast laser pulse excitation of a biased metal-semiconductor interface," *Appl. Phys. Lett.*, vol. 58, pp. 222-4, 1991.

[12] C. Fattinger and D. Grischkowsky, "Beams of Terahertz Electromagnetic Pulses," *OSA Proceedings on Picosecond Electronics and Optoelectronics*, vol. 4, pp. 225-231, 1989.

[13] J. Van Rudd and D. M. Mittleman, "Influence of substrate-lens design in terahertz time-domain spectroscopy," *J. Opt. Soc. Am. B*, vol. 19, pp. 319-329, 2002.

[14] P. U. Jepsen, R. H. Jacobsen, and S. R. Keiding, "Generation and detection of terahertz pulses from biased semiconductor antennas," *J. Opt. Soc. Am. B*, vol. 13, pp. 2424-2436, 1996.

[15] P. U. Jepsen and S. R. Keiding, "Radiation patterns from lens-coupled terahertz antennas," *Opt. Lett.*, vol. 20, pp. 807-809, 1995.

[16] W. Lukosz, "Light emission by magnetic and electric dipoles close to a plane dielectric interface. III. Radiation patterns of dipoles with arbitrary orientation," *J. Opt. Soc. Am.*, vol. 69, pp. 1495-503, 1979.

[17] R. W. P. King and G. S. Smith, *Antennas in Matter.* (Cambridge: MIT Press, 1981.)

[18] M. Born and E. Wolf, *Principles of Optics*, (7 ed. New York: Cambridge University Press, 1999.)

[19] M. T. Reiten, S. A. Harmon, and R. A. Cheville, "Terahertz beam propagation measured through three-dimensional amplitude profile determination," *J. Opt. Soc. Am. B*, vol. 20, pp. 2215-2225, 2003.

[20] J. W. Goodman, *Introduction to Fourier Optics*, (2nd ed. Boston: McGraw Hill, 1996).

[21] A. E. Siegman, *Lasers.* (Mill Valley: University Science Books, 1986).

[22] J. T. Verdeyen, *Laser Electronics.* (Englewood Cliffs: Prentice Hall, 1995).

[23] D. You and P. H. Bucksbaum, "Propagation of half-cycle far infrared pulses," *J. Opt. Soc. Am. B*, vol. 14, pp. 1651-1655, 1997.

[24] P. Kuzel, M. A. Khazan, and J. Kroupa, "Spatiotemporal transformations of ultrashort terahertz pulses," *J. Opt. Soc. Am. B*, vol. 16, pp. 1795-1800, 1999.

[25] V. I. Ar'nold, *Catastrophe Theory.* (Berlin: Springer-Verlag, 1992).

[26] L. Felsen, "Evanescent Waves," *J. Opt. Soc. Am.*, vol. 66, pp. 751-760, 1976.

[27] P. L. Marston, "Geometrical and Catastrophe Optics Methods in Scattering," in *Physical Acoustics*, vol. 21. (New York: Academic Press, 1992), pp. 2-221.

[28] J. A. Lock, "Semiclassical scattering of an electric dipole source inside a spherical particle," *J. Opt. Soc. Am. A*, vol. 18, pp. 3085-3097, 2001.

[29] M. T. Reiten, D. Grischkowsky, and R. A. Cheville, "Properties of surface waves determined via bistatic terahertz impulse ranging," *Appl. Phys. Lett.*, vol. 78, pp. 1146-1148, 2001.

[30] T. Poston and I. N. Stewart, *Catastrophe theory and its applications.* (London: Pitnam Publishing Ltd., 1978).

[31] G. Dangelmyer and W. Guttinger, "Topological approach to remote sensing," *Geophys. J. R. Astr. Soc.*, vol. 71, pp. 79-126, 1982.

[32] M. J. Gans, "Cross polarization in reflector type beam waveguides and antennas," *Bell Sys. Tech. Jour.*, vol. 55, pp. 289-316, 1976.

[33] J. C. G. LeSurf, *Millimetre-wave Optics, Devices, and Systems.* (Bristol: Adam Hilger, 1990).

[34] L. Allen and J. H. Eberly, *Optical resonance and two-level atoms.* (New York: John Wiley & Sons, 1975).

[35] B. R. Horowitz and T. Tamir, "Lateral displacement of a light beam at a dielectric interface," *J. Opt. Soc. Am.*, vol. 61, pp. 586-594, 1971.

[36] A. K. Ghatak, M. R. Shenoy, I. C. Goyal, and K. Thyagarajan, "Beam propagation under frustrated total internal reflection," *Opt. Comm.*, vol. 56, 1986.

[37] R. A. Cheville and D. Grischkowsky, "Far-infrared terahertz time-domain spectroscopy of flames," *Opt. Lett.*, vol. 20, pp. 1646-8, 1995.

[38] H. Harde, R. A. Cheville, and D. Grischkowsky, "Terahertz studies of collision-broadened rotational lines," *J. Phys. Chem. A*, vol. 101, pp. 3646-3660, 1997.

[39] H. Harde, R. A. Cheville, and D. Grischkowsky, "Collision-induced tunneling in methyl halides," *J. of Opt. Soc. Am. B-Optical Physics*, vol. 14, pp. 3282-3293, 1997.

[40] R. H. Jacobsen, D. M. MIttleman, and M. C. Nuss, "Chemical recognition of gases and gas mixtures with terahertz waves," *Opt. Lett.*, vol. 21, pp. 2011-2013, 1996.

[41] R. A. Cheville and D. R. Grischkowsky, "Far infrared foreign and self broadened rotational linewidths of high temperature water vapor," *J. Opt. Soc. Am. B*, vol. 16, pp. 317-322, 1998.

[42] R. A. Cheville and D. Grischkowsky, "Observation of pure rotational absorption spectra in the ν_2 band of hot H_2O in flames," *Opt. Lett.*, vol. 23, pp. 531-533, 1998.

[43] B. N. Flanders, R. A. Cheville, D. Grischkowsky, and N. F. Scherer, "Pulsed terahertz transmission spectroscopy of liquid $CHCl_3$, CCl_4, and their mixtures," *J. Phys. Chem.*, vol. 100, pp. 11824-35, 1996.

[44] J. T. Kindt and C. A. Schmuttenmaer, "Far-infrared Dielectric Properties of Polar Liquids Probed by Femtosecond THz Pulse Spectroscopy," *J. Phys. Chem.*, vol. 100, pp. 10373, 1996.

[45] T. I. Jeon and D. Grischkowsky, "Nature of conduction in doped silicon," *Phys. Rev. Lett.*, vol. 78, pp. 1106-1109, 1997.

[46] T. I. Jeon and D. Grischkowsky, "Characterization of optically dense, doped semiconductors by reflection THz time domain spectroscopy," *Appl. Phys. Lett.*, vol. 72, pp. 3032-3034, 1998.

[47] T. I. Jeon and D. Grischkowsky, "Observation of a Cole-Davidson type complex conductivity in the limit of very low carrier densities in doped silicon," *Appl. Phys. Lett.*, vol. 72, pp. 2259-2261, 1998.

[48] P. H. Bolivar, M. Brucherseifer, M. Nagel, H. Kurz, A. Bosserhoff, and R. Buttner, "Label-free probing of the binding state of DNA by time-domain terahertz sensing," in *Ultrafast Phenomena in Semiconductors 2001*, vol. 384-3, (Materials Science Forum, 2002), pp. 253-258.

[49] M. Nagel, P. H. Bolivar, M. Brucherseifer, H. Kurz, A. Bosserhoff, and R. Buttner, "Integrated THz technology for label-free genetic diagnostics," *Appl. Phys. Lett.*, vol. 80, pp. 154-156, 2002.

[50] R. Y. Chiao and A. M. Steinberg, "Tunneling times and superluminality," in *Progress in Optics*, vol. 37, (E. Wolf, Ed. Amsterdam: Elsevier, 1997), pp. 345-405.

[51] M. Mojahedi, E. Schamiloglu, K. Agi, and K. J. Malloy, "Frequency-domain detection of superluminal group velocity in a distributed Bragg reflector," *IEEE J. Quantum Electron.*, vol. 36, pp. 418-424, 2000.

[52] J. J. Carey, J. Zawadzka, D. A. Jaroszynski, K. Wynne, "Noncausal Time Response in Frustrated Total Internal Reflection?" *Phys. Rev. Lett.*, vol. 84, pp. 1431-1434, 2000.

[53] H. K. V. Lotsch, "Beam displacement at total internal reflection: The Goos-Hanchen effect II," *Optik Zeitschrft fur Licht und Elektronenoptik*, vol. 32, pp. 189-204, 1970.

[54] M. T. Reiten, D. Grischkowsky, and R. A. Cheville, "Optical tunneling of single-cycle terahertz bandwidth pulses," *Phys. Rev. E*, vol. 6403, 2001.

[55] B. E. A. Saleh and M. C. Teich, *Fundamentals of Photonics.* (New York: J. Wiley and Sons, 1991).

[56] R. Landauer and T. Martin, "Barrier interaction time in tunneling," *Rev. Mod. Phys.*, vol. 66, pp. 217-221, 1994.

[57] M. T. Reiten, K. McClatchey, D. Grischkowsky, and R. A. Cheville, "Incidence-angle selection and spatial reshaping of terahertz pulses in optical tunneling," *Opt. Lett.*, vol. 26, pp. 1900-1902, 2001.

[58] T. Tamir, "The Lateral Wave," in *Electromagnetic Surface Modes*, (A. D. Boardman, Ed. New York: John Wiley and Sons, 1982), pp. 521-548.

[59] P. Balcou and L. Dutriaux, "Dual optical tunneling times in frustrated total internal reflection," *Phys. Rev. Lett.*, vol. 78, pp. 851-854, 1997.

[60] J. Peatross, S. A. Glasgow, and M. Ware, "Average energy flow of optical pulses in dispersive media," *Phys. Rev. Lett.*, vol. 84, pp. 2370-2373, 2000.

[61] T. Martin and R. Landauer, "Time delay of evansecent electromagnetic waves and the analogy to particle tunneling," *Phys. Rev. A*, vol. 45, pp. 2611-2617, 1992.

[62] A. Ulman, *Characterization of Organic Thin Films.* (Boston: Butterworth-Heineman, 1995).

[63] D. M. Mittleman, S. Hunsche, L. Boivin, and M. C. Nuss, "T-ray tomography," *Opt. Lett.*, vol. 22, pp. 904-906, 1997.

[64] K. S. Lee, T. M. Lu, and X. C. Zhang, "The measurement of the dielectric and optical properties of nano thin films by THz differential time-domain spectroscopy," *Microelectronics Journal*, vol. 34, pp. 63-69, 2003.

[65] Z. P. Jiang, M. Li, and X. C. Zhang, "Dielectric constant measurement of thin films by differential time-domain spectroscopy," *Appl. Phys. Lett.*, vol. 76, pp. 3221-3223, 2000.

[66] Z. P. Jiang, X. G. Xu, and X. C. Zhang, "Improvement of terahertz imaging with a dynamic subtraction technique," *Appl. Opt.*, vol. 39, pp. 2982-2987, 2000.

[67] M. Brucherseifer, P. H. Bolivar, and H. Kurz, "Combined optical and spatial modulation THz-spectroscopy for the analysis of thin-layered systems," *Appl. Phys. Lett.*, vol. 81, pp. 1791-1793, 2002.

[68] S. Krishnamurthy, M. T. Reiten, S. A. Harmon, and R. A. Cheville, "Characterization of thin polymer films using terahertz time-domain interferometry," *Appl. Phys. Lett.*, vol. 79, pp. 875-877, 2001.

[69] J. L. Johnson, T. D. Dorney, and D. M. Mittleman, "Enhanced depth resolution is terahertz imaging using phase shift interferometry," *Appl. Phys. Lett.*, vol. 78, pp. 835, 2001.

[70] L. Duvillaret, F. Garet, and J. L. Coutaz, "Influence of noise on the characterization of materials by terahertz time-domain spectroscopy," *J. Opt. Soc. Am. B*, vol. 17, pp. 452-461, 2000.

[71] D. Guenther, *Modern Optics*, (2nd ed. New York: John Wiley & Sons, 1990).

[72] N. W. Ashcroft and N. D. Mermin, *Solid State Physics.* (New York: Holt, Rhinehart, and Winston, 1976).

[73] R. A. Cheville, R. W. McGowan, and D. Grischkowsky, "Time Resolved Measurements Which Isolate the Mechanisms Responsible for Terahertz Glory Scattering from Dielectric Spheres," *Phys. Rev. Lett.*, vol. 80, pp. 269-272, 1998.

[74] R. A. Cheville, R. W. McGowan, and D. R. Grischkowsky, "Late-time target response measured with terahertz impulse ranging," *IEEE Transactions on Antennas and Propagation*, vol. 45, pp. 1518-1524, 1997.

[75] R. W. McGowan, R. A. Cheville, and D. Grischkowsky, "First time measurement of the coupling efficiency of the surface wave on a dielectric cylinder via THz impulse ranging," presented at CLEO, Baltimore, MD, 1999.

[76] R. W. McGowan, R. A. Cheville, and D. Grischkowsky, "Direct observation of the Gouy phase shift in THz impulse ranging," *Appl. Phys. Lett.*, vol. 76, pp. 670-672, 2000.

[77] K. Kawase, J. Shikata, and H. Ito, "Narrow-linewidth tunable terahertz-wave sources using nonlinear optics," in Solid-State Mid-Infrared Laser Sources, vol. 89, *Topics in Applied Physics*, 2003, pp. 397-423.

[78] M. F. Kimmitt, "Restrahlen to T-rays - 100 years of terahertz radiation," *J. Biol. Phys.*, vol. 29, pp. 77-85, 2003.

[79] J. Z. Xu, C. L. Zhang, and X. C. Zhang, "Recent progress in terahertz science and technology," *Prog. Nat. Science*, vol. 12, pp. 729-736, 2002.

[80] A. G. Davies, E. H. Linfield, and M. B. Johnston, "The development of terahertz sources and their applications," *Phys. Med. Biol.*, vol. 47, pp. 3679-3689, 2002.

[81] T. Nagatsuma, "Photonic measurement technologies for high-speed electronics," *Meas. Sci. Tech.*, vol. 13, pp. 1655-1663, 2002.

[82] J. Shan, A. Nahata, and T. F. Heinz, "Terahertz time-domain spectroscopy based on nonlinear optics," *J. Nonlinear Opt. Phys. Mat.*, vol. 11, pp. 31-48, 2002.

[83] P. Y. Han and X. C. Zhang, "Free-space coherent broadband terahertz time-domain spectroscopy," *Meas. Sci. Tech.*, vol. 12, pp. 1747-1756, 2001.

[84] T. W. Crowe, J. L. Hesler, R. M. Weikle, and S. H. Jones, "GaAs devices and circuits for terahertz applications," *Infr. Phys. Tech.*, vol. 40, pp. 175-189, 1999.

[85] G. M. Rebeiz, "Millimeter-Wave and Terahertz Integrated-Circuit Antennas," *Proc. IEEE*, vol. 80, pp. 1748-1770, 1992.